Article:
Gómez Martín, JC, Vömel, H, Hay, TD et al. (5 more authors) (2016) On the variability of ozone in the equatorial eastern Pacific boundary layer. Journal of Geophysical Research: Atmospheres, 121 (18). pp. 11086-11103. ISSN 2169-897X

https://doi.org/10.1002/2016JD025392

On the Variability of Ozone in the Equatorial Eastern Pacific Boundary Layer

J. C. Gómez Martín[1†*], H. Vömel[2], T. D. Hay[1], A. S. Mahajan[1‡], C. Ordóñez[1¶], M.C. Parrondo Sempere[3§], M. Gil-Ojeda[3], and A. Saiz-Lopez[1]

1. Department of Atmospheric Chemistry and Climate, Institute of Physical Chemistry Rocasolano, CSIC, Madrid, Spain.

2. Earth Observing Laboratory, National Center for Atmospheric Research, Boulder, USA.

3. Atmospheric Research and Instrumentation Branch, National Institute for Aerospace and Technology (INTA), Madrid, Spain.

† Now at: School of Chemistry, University of Leeds, Leeds, UK.

‡ Now at: Indian Institute of Tropical Meteorology, Pune, India

¶ Now at: Dpto. Física de la Tierra II, Facultad de Ciencias Físicas, Universidad Complutense de Madrid, Madrid, Spain.

§ Now at: Space Programs and Systems Department, National Institute for Aerospace and Technology (INTA), Madrid, Spain

* Correspondence to: J.C. Gómez Martín (chmjgm@leeds.ac.uk)

Key points:

- First continuous, long term measurements of ozone in the Equatorial Eastern Pacific Boundary Layer.
- Analysis and interpretation of the diurnal and seasonal cycles.
- Description of ozone intraseasonal variability and posible link to Tropical Instability Waves

Abstract

Observations of surface ozone (O_3) mixing ratios carried out during two ground-based field campaigns in the Galápagos Islands are reported. The first campaign, PIQUERO (Primera Investigación sobre la Química, Evolución y Reparto de Ozono) was carried out from September 2000 to July 2002. The second study, CHARLEX (Climate and HAlogen Reactivity tropicaL EXperiment), was conducted from September 2010 to March 2012. These measurements complement the SHADOZ ozonesonde observations made with weekly to monthly frequency at Galápagos. In this work, the daily, intraseasonal, seasonal and interannual variability of O_3 in the marine boundary layer are described and compared to those observed in other tropical locations. The O_3 diurnal cycle shows two regimes: *i*) photochemical destruction followed by nighttime recovery in the cold season (July to November), and *ii*) daytime advection and photochemical loss followed by nighttime depositional loss associated to windless conditions in the warm season (February to April). Wavelet spectral analysis of the intraseasonal variability of O_3 reveals components with periods characteristic of Tropical Instability Waves. The O_3 seasonal variation in Galápagos is typical of the Southern Hemisphere, with a maximum in August and a minimum in February-March. Comparison with other measurements in remote tropical ocean locations shows that the change of the surface O_3 seasonal cycle across the Equator is explained by the position of the Inter-Tropical Convergence Zone and the O_3 levels upwind.

1. Introduction

In the last 40 years a wealth of data has been accumulated from measurements of surface ozone (O_3) and vertical profiles at multiple observatories in remote locations around the globe. For instance, surface measurements at stations of the U.S. Geophysical Monitoring for Climate Change (GMCC) network started 40 years back [*Oltmans and Levy II*, 1994], and the Southern Hemisphere ADditional OZonesondes (SHADOZ) program [*Thompson et al.*, 2011] has collected and made public ozonesonde data acquired at tropical locations since 1998. Also numerous ship- and aircraft-based atmospheric observations of trace gases relevant for the tropospheric O_3 budget have been carried out since the seventies (eg. [*Fabian and Pruchniewicz*, 1977; *Piotrowicz et al.*, 1986; *Winkler*, 1988; *Johnson et al.*, 1990; *Paluch et al.*, 1995; *Gregory et al.*, 1996; *Schultz et al.*, 1999; *Browell et al.*, 2001; *Wang et al.*, 2001; *Shiotani et al.*, 2002; *Conley et al.*, 2011]). These measurements have enabled comprehensive studies of the background atmosphere, which have elucidated the main mechanisms controlling the natural O_3 budget and its variability across different time scales. Despite of the fact that O_3 and trace gas observations are still limited and sparse over the open ocean, a better picture of global O_3 distribution is now available, which permits assessing more confidently changes that may be attributed to human activity.

Globally, the remote marine boundary layer (MBL) and in particular the Tropical Pacific MBL is an atmospheric O_3 sink. The existence of an equatorial surface O_3 minimum has been demonstrated by several research cruises [*Piotrowicz et al.*, 1986; *Winkler*, 1988; *Johnson et al.*, 1990]. In this low NO_x regime, the O_3 budget is determined by transport and its main photochemical losses. The daily variability of

the O_3 profile shows a characteristic pattern encompassing photochemical daytime depletion and night time replenishment [*Johnson et al.*, 1990; *Oltmans and Levy II*, 1994; *Ayers et al.*, 1997; *Dickerson et al.*, 1999; *Nagao et al.*, 1999; *de Laat and Lelieveld*, 2000; *Hu et al.*, 2010]. Photochemical losses are dominated by O_3 photolysis followed by the $H_2O + O^1D$ reaction, and HO_x reactions [*Liu et al.*, 1983; *Thompson et al.*, 1993]. This loss mechanism is favored by high insolation over warm sea water and is subjected to seasonal changes. In remote locations the maximum amplitude of the daily cycle is associated to the insolation maximum, although this may be obscured by seasonal continental outflows [*Oltmans and Levy II*, 1994]. Higher O_3 mixing ratios also tend to favor larger amplitudes of the daily cycle, since O_3 depletion depends on odd oxygen radicals generated by O_3 photolysis [*de Laat and Lelieveld*, 2000]. The contribution of halogens emitted from the ocean surface to O_3 depletion in the MBL and the free troposphere (FT) has also been quantified [*Dickerson et al.*, 1999; *Read et al.*, 2008; *Saiz-Lopez et al.*, 2012]. The photochemical lifetime of O_3 in the Equatorial Pacific MBL has been estimated to be of the order of 6.5 days [*Conley et al.*, 2011]. Surface O_3 sources are horizontal transport [*de Laat and Lelieveld*, 2000], entrainment from the FT [*Ayers et al.*, 1997; *Hu et al.*, 2010; *Conley et al.*, 2011] and some limited NO_x chemistry.

The impact of convection on free-tropospheric O_3 is apparent in the structures of moist, low O_3 layers sandwiched between dry, high O_3 layers frequently found in ozonesonde profiles and aircraft surveys, resulting from convection followed by horizontal advection in the middle troposphere [*Shiotani et al.*, 2002]. Due to the link between water vapor and O_3, and to enhanced convection, the seasonal cycle of MBL and tropospheric O_3 in the tropical Pacific [*Thompson et al.*, 2003] is related to the sea surface temperature (SST) seasonal variation. On interannual time scales, ENSO is

77 the dominant mode of tropical tropospheric O_3 variability [*Ziemke et al.*, 2010; *Randel*
78 *and Thompson*, 2011]. Chemical transport models (CTM) driven by meteorological
79 reanalysis fields reproduce the main features of locally observed seasonal variations
80 in O_3 [*Wei et al.*, 2002] as well as the ENSO-related interannual variability and the
81 intraseasonal variability of the tropospheric column O_3 (TCO) above the Pacific
82 [*Ziemke et al.*, 2015]. By contrast, chemistry climate models (CCM), usually
83 constrained by SST observations, reproduce ENSO interannual variability, but
84 struggle to reproduce shorter time scale changes [*Oman et al.*, 2011; *Ziemke et al.*,
85 2015].

86 The intraseasonal variability of tropospheric O_3 in the Pacific has been studied using
87 satellite data and it has been found to contain the signature of the Madden-Julian
88 Oscillation (MJO) [*Ziemke et al.*, 2015]. MBL O_3 variability on this time scale is
89 perhaps not as well studied, mainly due to the sparse spatial coverage of observatories
90 and sparse time coverage inherent in ship and aircraft campaigns. Continuous
91 measurements at specific locations are required to observe changes related to
92 oscillation patterns such as the MJO. For example, continuous surface measurements
93 at Samoa display a ~15 day period pattern throughout the year [*Oltmans and Levy II*,
94 1994], which remains to be studied in detail. A previous study of selected sections of
95 this dataset did not reach firm conclusions about the cause of such variability
96 [*Piotrowicz et al.*, 1991], but suggested that large-scale circulation patterns could
97 determine the characteristics of the Equatorial Western Pacific O_3 minimum.

98 In this paper, the first ground-based continuous observations of surface O_3 in the
99 Eastern Tropical Pacific are reported. The first part of these observations was carried
100 out in the period 2000-2002, and a second set of measurements was acquired 10 years

101 later in the period 2010-2012. The variability of O_3 on the daily, intraseasonal and
102 seasonal time scales is investigated and discussed in the context of background O_3 in
103 the tropical MBL across the globe.

104 **2. Instrumentation**

105 A summary plot of the two campaigns is presented in Fig. 1, showing surface O_3 daily
106 averages and surface ozonesonde measurements plotted alongside concurrent satellite
107 and in situ SST observations for seasonal contextualization. The SHADOZ program
108 started regular ozonesoundings at San Cristóbal, Galápagos (Ecuador) in March 1998
109 and is ongoing up to the present, albeit with some interruptions. This program was
110 augmented by the PIQUERO (Primera Investigación sobre la Química, Evolución y
111 Reparto de Ozono) project, which measured surface O_3 at San Cristóbal from
112 September 2000 through July 2002. Vertical profiles were measured using standard
113 Electrochemical Concentration Cell (ECC) ozonesondes [*Thompson et al.*, 2007].
114 Surface O_3 was measured using an ultraviolet absorption (UV) detector (2B
115 Technologies, serial number 16), which was co-located with the ozonesonde launch
116 program at the meteorological observatory at San Cristóbal (0.90° S, 89.61° W). The
117 inlet of the surface O_3 monitor at the meteorological observatory was placed 1 m
118 above the roof of the two story observing building and approximately 14 m above
119 mean sea level using Teflon tubing to the instrument. The SHADOZ ECC
120 measurements at the surface were employed to validate the UV measurements (Fig. 2,
121 top panel). Based on this comparison, UV data from 15 April 2001 to 24 May 2001
122 and 29 March 2002 to 25 April 2002 has been removed due to values exceeding
123 systematically the contemporary ECC measurements by more than a factor of 2,
124 which is possibly due to a local pollution source. Meteorological measurements

carried out at the observatory from 2000 through 2002 include air temperature, wind speed (WS) and relative humidity (RH). Only monthly averages of SST are available for the 2000-2010 period.

CHARLEX (Climate and HAlogen Reactivity tropicaL Experiment) was a ground-based study of the composition and chemistry of the MBL carried out at Puerto Villamil, Isabela Island (0.96° S, 90.97° W) from September 2010 to June 2011, and at the meteorological observatory in San Cristóbal from July 2011 to February 2012 [*Gómez Martín et al.*, 2013] (see Fig. 1). Its main goal was to study the temporal evolution of reactive halogens in the Eastern Pacific MBL. Combined with spatially resolved data from the same region [*Mahajan et al.*, 2012] and other locations around the world [*Prados-Roman et al.*, 2015], the results of CHARLEX have provided new field insights into the emission of reactive iodine precursors from the ocean [*Carpenter et al.*, 2013; *MacDonald et al.*, 2014] and the contribution of iodine and bromine to surface O_3 depletion [*Saiz-Lopez et al.*, 2014]. A detailed description of the measurement sites can be found in [*Gómez Martín et al.*, 2013]. Surface O_3 measurements were performed with two UV absorption detectors (2B Technologies, models 202 and 205, accuracy 1.5 and 1.0 ppbv respectively), one of which was sent for refurbishing and recalibration to the manufacturer during the campaign and then sent back for replacing the other a month later. At Isabela, the Teflon tubing inlet was guided using a pole pointing southward, sampling air 2 m away from the laboratory walls and about 5 m directly above sea level. In San Cristóbal the inlet was set up in a similar manner on the top of a two storey building (5 m above ground level) within the Meteorological Station compound. Data was acquired every two seconds and continuously logged into a computer. The data was subsequently averaged in 10 minute bins for preliminary analysis and quality control and finally one hour averages

and the one day averages, shown in Fig. 1, were calculated for the analysis presented in this paper. A wealth of ancillary data were acquired in situ during the campaign (meteorological variables, NO_x, global irradiance) [*Gómez Martín et al.*, 2013]. A set of ozonesondes (Science Pump Corp, Model 6A) was launched mainly during the warm season in 2011 (see Fig. 1), which was necessary because the SHADOZ program at San Cristóbal had been interrupted in 2008. The ozonesondes were attached to meteorological radiosondes (Väisala), which provided pressure, temperature and humidity data. The entire system was flown on a TOTEX balloon (TX-1200) filled with helium. Chemical sensing solutions were prepared following the manufacturer's recommendations. The standard cathode solution used was 1% KI buffered [*Komhyr et al.*, 1995]. An O_3 generator (Science Pump Corporation, TSC-1) was used for calibration and preparation of the sondes [*Komhyr*, 1986]. Laboratory studies indicate that ECC ozonesondes operated according to standard procedures yield 3-5% precision and 5-10% accuracy up to 30 km altitude [*Smit et al.*, 2007]. Simultaneous ozonesondes launched from Isabela and San Cristóbal at 12:00 Local Time (LT) during April and May 2011 were essentially in agreement and showed that the vertical structure of the MBL and the lower Free troposphere (LFT) above the two locations is similar. A collection of co-located ECCs was used as surface instruments to validate the UV absorption measurements in the period when the surface monitors were replaced, with both techniques being in good agreement (Fig. 2, bottom panel).

The SHADOZ O_3 profiles obtained at San Cristóbal between 1998 and 2012 [*Thompson et al.*, 2003] have been employed to contextualize the O_3 measurements at Galápagos. Contemporary remote sensing observations from MODIS Terra (2000–2002) and MODIS Aqua (2002–2012), as well as the NOAA OI SST V2 High Resolution Dataset (1981-present) [*Reynolds et al.*, 2007], have been used for

investigating connections between surface O_3 and SST. The averaging regions or 'boxes' of MODIS SST satellite data around Galápagos are shown in Fig. 2*a* of [*Gómez Martín et al.*, 2013] and also defined in the supplementary information of the present work (Table S1). To compensate for the lack of daily meteorological and SST data at San Cristóbal during PIQUERO, records belonging to other locations such as the Charles Darwin Station at Santa Cruz Island (0.75° S, 90.32° W) and the two easternmost equatorial TAO buoys (0° and 2° S, 95° W) [*McPhaden et al.*, 2009] have been compiled.

3. Observations

The regional climate around the Galápagos Archipelago is determined by the interaction of ocean currents and winds, governed by the seasonal shift of the ITCZ, and strongly influenced by ENSO. The year is divided climatologically into two seasons: the rainy and warm season lasting from January-February through April, and the dry colder season lasting the remainder of the year [*Alpert*, 1963]. This division does not only determine the O_3 seasonal cycle but also modulates the intraseasonal and the daily variability.

3.1. Daily variability

The O_3 daily cycle in the Galápagos has two distinct regimes. From July through November, i.e. during the cold season and when O_3 seasonal maximum occurs, a photolytic destruction regime is observed, with O_3 peaking early in the morning (7:00-8:00 LT), decaying during the day, and recovering during the night (the average daily profile of the two campaigns for September-November is shown in Fig. 3*a* as a solid black line with black circles). A permanent strong inversion exist during the cold

198 season (see section 3.3), which suggest that advection is the main mechanism for
199 night-time O_3 replenishment [*de Laat and Lelieveld*, 2000]. Trajectory analysis shows
200 that air masses spend several days over the Pacific cold tongue before being advected
201 into the Galápagos area [*Sorribas et al.*, 2015]. Note in Fig. 3*a* that a small increase of
202 O_3 is observed between 6:00 and 7:00 LT, which corresponds to peak NO_2 levels of
203 ~100 pptv early in the morning. Some rush hour anthropogenic emissions close to the
204 site caused by ship traffic were observed on the spot, but the NO_2 cycle is driven
205 mainly by radiation. The evening peak gives an idea of the total NO_x levels, which are
206 at the limit of what normally is considered a low-NO_x environment [*de Laat and*
207 *Lelieveld*, 2000]. The average O_3 daytime decrease for the two campaigns in the cold
208 season is ~1 ppbv day^{-1}. The monthly average daytime decrease for October 2010 is
209 2.3 ppbv day^{-1} (solid black line in Fig. 3*a*). This daily cycle may also appear during
210 the transition months between the warm and the cold seasons (May-July, November-
211 January), although generally a flat profile is observed. The estimated contribution of
212 HO_x photochemistry to O_3 photochemical loss is ~70% [*Gómez Martín et al.*, 2013],
213 with the rest corresponding to halogens (IO_x and BrO_x).

214 The amplitude of the daily cycle at Galápagos also has some interannual variability.
215 Fig. S1 shows the time series of monthly averaged daily O_3 loss from 7:00 LT to
216 17:00 LT. Net photolytic O_3 destruction (black squares, negative values) was
217 observed through the cold seasons of 2000, 2001 and 2010. In 2011 photolytic O_3 loss
218 was only seen in July and not in the following months, when a large cold season
219 negative anomaly occurred (see interannual variability, section 3.4).

220 In the warm months (February through April, Fig. 3*b*), and sometimes in the
221 preceding transition period (end of December and January), a completely different O_3

222 daily cycle emerges, which appears to be mainly driven by the wind daily cycle.
223 Figure 3*b* (blue line) shows that during night time the wind is very low. Surface dry
224 deposition to the land surface surrounding the measurement site during the windless
225 periods is therefore a primary cause of the observed nighttime O_3 reduction. At dawn,
226 wind starts blowing again from the south and flushes the stagnant air mass bringing
227 O_3-richer open ocean air, causing a 5-6 ppb increase between 6:00 LT and 10:00 LT.
228 The replenishment of O_3 is followed by day-time photochemical destruction. The
229 relative changes between 10:00 and 17:00 LT are similar between Figs. 3*a* and 3*b*,
230 suggesting similar photochemical destruction in the warm and cold period.

231 The higher levels of NO_x in the warm period (the green squares in Fig. 3*b* correspond
232 to NO_2) are possibly due to the increase in ship traffic during the peak tourist season,
233 while the higher NO_2 nighttime levels (0.4 ppb) may result from a combination of
234 increased fuel consumption and the low winds. NO_2 and NO spikes of the order of 1
235 ppb are observed in the early morning and the evening. The reaction of O_3 with NO is
236 probably responsible for the absence of nighttime NO. This may also contribute to the
237 removal of O_3, although the NO_2 levels observed are lower than the O_3 nighttime
238 depletion (~4 ppb), which shows that this cannot be the main O_3 sink. The correlation
239 coefficients between nighttime (18:00-5:00 LT) O_3, NO_2 and wind speed in the
240 January-April 2011 period are $R(O_3\text{-}NO_2)$ = -0.434, $R(O_3\text{-WS})$ = 0.425 and $R(NO_2\text{-}$
241 WS) = -0.571 ($p < 0.01$). Visual inspection of the hourly averaged data confirms that
242 some very low O_3 (even complete destruction) events coincide with high NO_x
243 episodes (up to 3 ppbv), but also that high NO_x episodes with non-zero wind do not
244 lead to large nighttime O_3 depletion. Thus it can be concluded that low wind favors
245 accumulation of NO_x and depletion of O_3, but ultimately it is another process (most
246 likely dry deposition to the land surface) what leads to the O_3 loss. Fig. 3 also shows

247 some evidence of transient O_3 production related to the high NO_x early morning and
248 evening events. Fig. 3*a* shows a sharper increase of O_3 between 6:00 LT and 7:00 LT
249 in October. The onset of O_3 increase in the February average in Fig. 3*b* matches very
250 well the onset of wind, but the February-April average (black dots) shows that some
251 O_3 production (~1 ppb) occurs at dawn between 5:00 LT and 7:00 LT during the NO_x
252 spike before the wind starts blowing at 7:00 LT. There is also some indication in Fig.
253 3*b* that the NO_x spike in the evening forms some extra O_3 just before dusk. In any
254 case, it seems clear from the data in Fig. 3 that advection is the major source of O_3
255 during the warm season.. It is worth noting that despite the large O_3 increase between
256 6:00 and 8:00 LT, the total mixing ratios are still very low, at levels similar to those at
257 Samoa [*Oltmans and Levy II*, 1994]. Fig. S1 shows the time series of monthly
258 averages of daily advection of O_3 between 5:00 LT and 10:00 LT. It can be seen that
259 the deposition-advection process occurs systematically from February to April (red
260 squares, positive values).

261 Fig. 4 shows average vertical profiles for some of the most frequent launching times
262 at Galapagos from the SHADOZ database, with August-October averages plotted in
263 panel *a* and February-April averages in panel *b*. In the warm season the profile at 6:00
264 LT reaches the highest MBL O_3 at 1 km and the lowest at the surface. The departure
265 of the 6:00 LT profile from the dependence on altitude of the daytime profiles below
266 0.6 km reinforces the conclusion that O_3 is depleted near the surface around the
267 measurement site during nighttime due to the low surface wind regime. By contrast,
268 the cold season profiles are roughly in the same order though the MBL and the
269 inversion layer (IL). Panel *d* in Fig. 4 shows daily profiles from the ozonesondes at
270 selected heights for February-April, emphasizing the distinct behavior at the surface
271 in the warm season, which contrasts with photochemical depletion between 0.6 and 2

272 km. The daily variation in the cold season is fairly homogeneous through the MBL,
273 with photochemical production between 6:00 and 8:00 LT, followed by
274 photochemical destruction through the day and recovery in the evening.

275 **3.2. Intraseasonal variability**

276 ***Surface data correlations in the frequency and time domains***

277 The daily averages of SST and O_3 in Fig. 1 contain oscillations with amplitude of up
278 to 4 ºC and 10 ppbv respectively within periods of 2-4 weeks. The intraseasonal
279 variability can be better visualized by applying a five day running average to the daily
280 average time series in order to remove noise, and then subtracting the monthly
281 average from the daily average time series. The resulting datasets for surface O_3 and
282 H_2O vapor mixing ratios, wind meridional component (v) and SST during CHARLEX
283 are shown in Fig. 5. O_3 peaks separated by 15-30 days are concurrent with SST and
284 water vapor minima.

285 Due to the non-stationary nature of time series of atmospheric and oceanic variables
286 (amplitude and phase varying with time), wavelet analysis is a suitable technique for
287 spotting their underlying oscillation patterns and resolve their amplitude variations
288 with time. Fig. 6 shows the power wavelet spectrum [*Torrence and Compo*, 1998] of
289 O_3 (panel *a*) and in situ SST (panel *b*) during CHARLEX, and the O_3-SST cross
290 power wavelet spectrum (panel *c*) and wavelet coherence (panel *d*) [*Grinsted et al.*,
291 2004] for the CHARLEX campaign. Relative phase is shown as arrows (in-phase
292 pointing right, anti-phase pointing left and 90° pointing down). During CHARLEX,
293 O_3 and SST have oscillations with periods between 15 and 33 days (Fig. 5, panels *a*
294 and *b*). Global wavelet spectra and time series of variance in selected frequency

295 ranges are useful to visualize this variability. The global wavelet spectra for O_3 (Fig.
296 S2) and satellite and in situ SST (Fig. S3 and S4 respectively) have peaks 95%
297 significant against red noise for periods of 17 and 33 days, and 17, 33 and 56 days,
298 respectively.

299 Besides the observation of significant frequency components in different variables, it
300 is important to stablish if these are simultaneous and coherent. There is significant O_3-
301 SST common power in the ~15 and ~30 day bands, mainly during the two cold
302 seasons (Fig. 6, panel *c*). Significant coherence also exist for these bands (Fig. 6,
303 panel *d*), from the beginning of the measurements to the end of November 2010 and
304 between mid-July and early November 2011. There is significant cross power around
305 the 16 day period in January-February 2011, but no coherence. Significant coherence
306 seems then to be restricted to the cold season, even though significant cross power
307 also exist in the early warm season. Within the intervals of significant cross-power
308 and coherence, the phase lag is 180-225° in the 15 and 30 day bands in the cold
309 season of 2010, while in the cold season of 2011 is ~90° and ~225° in the 17 and 30
310 day bands, respectively. The wavelet spectra and cross-spectral relationships of O_3
311 and H_2O mixing ratios for the CHARLEX period are shown in Fig. S5. The picture is
312 very similar to that in Fig. 6, and in fact SST and H_2O have significant cross-power
313 and squared coherence and are in phase in both cold seasons of the CHARLEX
314 campaign. The generally antiphase behaviour of O_3 and SST (H_2O) in the frequency
315 domain has its time domain counterpart in negative correlation between this variables
316 (see below), as suggested by Fig. 4, and it fits with the fact if that water vapour
317 increases, this may enhance O_3 photolytic depletion.

Fig. S6 shows the corresponding wavelet spectra for PIQUERO in the period 09-2000 to 03-2002 (with an interruption in between). Unfortunately, discontinuities in the data preclude an analysis of the whole campaign, and a good part of both cold seasons are impacted by the data edges. The results for the PIQUERO period do not show the same features than in the CHARLEX period, or at least not as clearly. Significant oscillations in O_3 and SST are missing in the cold season of 2000. But, on the other hand, O_3 oscillations have significant power in the 17 and 33 day bands in the cold season of 2001. SST significant power in these bands falls in the cone of influence region. Significant cross-power exists from October to December. In the warm season of 2001, significant power between 8 and 20 day periods is observed in O_3. This high variability precedes the period from 15 April 2001 to 24 May 2001 screened due to factor of 2 deviations with respect with the collocated ECCs at San Cristóbal (see section 2). This high frequency variability was not observed at Isabela Island.

In order to show how these frequency relationships translate into the time domain, correlation coefficients between the anomalies of surface O_3 and other variables have been computed (Table S1). Correlation coefficients have been determined for the entire period of measurements, for all the cold (warm) season periods together and for each individual season. When the complete time series or the warm season sub-sets are considered, the correlations between O_3 and other variables are poorer or less significant than for the cold (warm) seasons sub-sets considered together or individually. Enhanced correlations for separated seasons and the anti-correlation of SST and O_3 in the cold periods reflect the time-dependent frequency and phase relationships described above. However, these correlation coefficients are generally smaller than 0.5, so these variables explain individually only a small fraction of the O_3 variability. Results of multivariate linear regression of O_3 anomalies vs. the available

343 environmental and meteorological variables are listed in Table 1. This analysis yields
344 more than one significant regression coefficient for cold season data segments. The
345 most significant increase in the explained variance of O_3 anomalies with respect to the
346 simple correlations in Table S1 occurs for the first CHARLEX cold season, where the
347 explained variance rises from 32% with only water vapor to 59% by adding linear
348 terms to the regression (v, SST, Rad and NO_2). Note that this is the only period of the
349 campaign during which all in situ variables were measured.

350 ***Intraseasonal variability in the vertical distribution of ozone***

351 The low sampling rate of the SHADOZ ozonesondes (average of three sondes per
352 month between 1998 and 2008) precludes a study of the weekly to monthly variability
353 of the O_3 profile using spectral analysis techniques. However, during the PIQUERO
354 period and the year before, the number of ozonesondes launched was higher (weekly).
355 Fig. 7 (and Fig. S7) show contour plots of O_3 vertical distribution vs. time (panels *a*
356 and *d*), surface O_3 (panels *b* and *e*) and SST (panels *c* and *f*). The figures include
357 examples for two cold periods (warm periods in Fig. S7). The altitude of the main
358 inversion (altitude of maximum absolute lapse rate) is overlaid on the O_3 contour plot.
359 Inspection of Fig. 7 reveals ~20-30 day period oscillations on the structure of the
360 MBL and FT at different altitudes. In 2000, the inversion height (black circles)
361 changes roughly following the oscillations of SST. The O_3 mixing ratios within the
362 MBL and the IL experiences oscillations as well. Using the data in Fig. 7*d-f* in the
363 period where oscillations are observed (J153 - J337, i.e. from 1 June to 2 December
364 2000), the correlation coefficient between the O_3 anomalies (0-300 m average) and
365 MBL height is R = -0.432 (p = 0.022). This increases to R = -0.610 (p = 0.006) for the
366 J153 - J265 period (1 June - 21 September). Correlation of MBL height with SST is

also significant: R = -0.568 (p=0.014) for J153 - J265. The anti-correlation between O_3 and SST anomalies (i.e. the blue dots in Fig. 7*e* and Fig. 7*e*) is weak and not significant at 95% level, except if the data point at J272 is screened. The data in Fig. 7*a-c* (1999) shows significant correlation between O_3 and SST anomalies in the J189-J301 period (R = -0.497, p = 0.016), but no significant correlation between SST and MBL height. The ozonesonde data for the cold period of 2001 does not show significant correlations. In Fig. 8, the averaged air temperature, O_3 mixing ratio and RH vertical profiles corresponding to negative and positive anomalies of SST during the cold season of 2000 (Marked with triangles in Fig. 7*e-f*) are compared. It can be seen that low surface O_3 coincides with a higher inversion (by up to ~500 m, Fig. 8, panel *a*) and higher water content of the MBL (panel *c*).

Fig. S7 shows how in the Eastern Pacific warm season (March-May) the height of the inversion and the O_3 mixing ratios are not correlated to variations of SST. An alternation of periods of capped/uncapped MBL occurs separated by ~20 days, and the absence of inversion is generally associated with a decrease of O_3 through the MBL-IL-LFT column due to convection.

3.3. Seasonal variability

Fig. 9 shows average vertical profiles of T (panel *a*), O_3 (panel *b*), and RH (panel *c*) for March, June, September and December. The annual cycles of O_3 and H_2O mixing ratios in the MBL, the IL and the LFT using the full SHADOZ dataset (1998-2014) plus the CHARLEX ozonesondes (2011) are shown in Fig. 9, panels *d* and *e* respectively. The annual cycles of inversion height and lapse rate calculated from ozonesonde data are plotted in Fig. 9*f*. The cycles of surface wind and SST are plotted in Fig. 10, panels *g* and *h* respectively. The IL is defined here by the interval of

positive lapse rates (-dT/dz) around the altitude of the maximum lapse rates, while the MBL and the LFT are defined as the layers between the surface and the IL and between the IL and 4 km, respectively.

Seasonal anti-correlation between surface O_3 and SST (R = -0.848) and H_2O (R = -0.882) and positive correlation with wind (R = 0.719, mostly with v) can be seen in Fig. 9 (*d* and *e*) and Fig. 10 (*e* - *h*). Surface O_3 is also anti-correlated with the inversion layer height and positively correlated with the lapse rate (Fig. 9, panel *f*). The seasonal variation of O_3 in the MBL, IL and FT shows a secondary maximum in the warm season that is not observed at the surface. The water vapor mixing ratio only shows a strong seasonal dependence in the MBL.

For the purpose of comparison with seasonal cycles in other locations [*Parrish et al.*, 2016], a sine function of the form $y = y_0 + A_1 \sin(\chi + \phi_1) + A_2 \sin(\chi + \phi_2)$ has been fitted to the seasonal cycles of O_3 in Fig. 9*b*. This is equivalent to derive a Fourier series expansion with a fundamental and a second harmonic term. The resulting parameters for surface O_3 are: y_0 = 12.8 ± 0.5 ppbv, A_1 = 5.3 ± 0.8 ppbv, ϕ_1 = -2.74 ± 0.13 rad, A_2 = 0.8 ± 0.7 ppbv, and ϕ_2 = -0.7 ± 1.0 rad (95% confidence limits). The increase in the quality of the fit by including a second harmonic is marginal (R = 0.986 vs R = 0.972). The seasonal cycle above the surface presents a significant second harmonic component. The fitted parameters for the LFT O_3 cycle are: y_0 = 24.2 ± 0.3 ppbv, A_1 = 4.4 ± 0.4 ppbv, ϕ_1 = 2.69 ± 0.09 rad, A_2 = 3.0 ± 0.4 ppbv, and ϕ_2 = -1.21 ±0.14.

3.4. Interannual variability

Fig. 10 shows composites or continuous series of deseasonalized monthly averages of

414 O_3, water vapor, WS, and SST. The O_3 series has been constructed by concatenating
415 the SHADOZ monthly averages with the monthly averages of the data acquired
416 during the CHARLEX campaign. The surface data acquired during the PIQUERO
417 campaign (filtered as explained in section 2) is averaged with the SHADOZ data
418 obtained during the same period to obtain the corresponding monthly averages. The
419 water vapor, wind speed and SST monthly averages are calculated from the
420 measurements at San Cristobal. The correlation between O_3 and the other series in
421 Fig. 10 is not larger than 0.5 but statistically significant at the 99% confidence level.
422 The sign of correlation with SST (Fig. 10*d*) and water vapor (Fig. 10*b*) is negative.
423 Regression of O_3 against several variables does not enhance the amount of explained
424 variance beyond 25%.

425 **4. Discussion**

426 **4.1. Daily variability**

427 Of all tropical and sub-tropical stations where data is available, Samoa is the one
428 resembling more closely the behavior of surface O_3 at Galápagos, except for the
429 February-April warm period. In Samoa there is a small seasonal dependence of the
430 amplitude of the daily cycle, which is larger in June-November (~2 ppbv), coincident
431 with the insolation and the O_3 maxima. Higher O_3 mixing ratios tend to favor larger
432 amplitudes of the daily cycle because the primary removal mechanism (photolysis and
433 reaction of O^1D with water) is first order in O_3. In Galápagos, net photolytic
434 destruction peaked in the cold season of 2000, 2001 and 2011 (Fig. S1, black squares
435 negative values). The small amplitude of the daily cycle in August-November 2011 is
436 possibly related to the generally low O_3 mixing ratios during the 2011 cold season.

437 The O_3 daily cycle in Galápagos during the warm season resembles the daily cycle
438 and absolute levels observed at Paramaribo (Suriname, 6° N , 55° W) through the year
439 [*Maas*, 2004]. The actual background surface O_3 levels in the warm season are
440 obscured by the losses caused by nighttime stagnation of the sampled air masses. The
441 amplitude of the seasonal cycle at a similar location such as Samoa is 10 ppbv (Fig.
442 11), which suggests that the average O_3 in the warm season at Galápagos could be
443 around 8-9 ppbv using the seasonal O_3 maximum as a reference. Extrapolation of the
444 average vertical profiles at 8:00 and 12:00 LT (Fig. 4, panel *a*) from 0.6 km
445 downwards also suggests average surface values around 7-10 ppbv, i.e. between the
446 night time minimum and the daytime maximum. Thus, daily averages of the surface
447 UV measurements, and also monthly averages of ECC measurements combining
448 launch times before and after 6:00 LT, may not be far from the background O_3 mixing
449 ratios.

450 Of those ozonesondes launched at San Cristóbal from January to April, 28 were
451 launched between 5:00 and 7:00 LT and 45 were launched between 8:00 and 18:00
452 LT. Measurements taken during the low wind periods at night during warm months
453 show systematically lower O_3 mixing ratios (Fig. S8) and cannot be considered as
454 representative of the oceanic background conditions

455 **4.2. Intraseasonal variability**

456 The oscillation periods observed in the O_3 daily anomalies in the cold season are close
457 to the periods of Tropical Instability Waves (TIWs) [*Legeckis*, 1977; *Chelton et al.*,
458 2000]. TIWs are westward propagating non-stationary waves with 17 day period and
459 1 m s^{-1} phase speed near the Equator, and 33-day period and 0.5 m s^{-1} phase speed
460 north of the Equator [*Lyman et al.*, 2007]. They are caused by meridional and vertical

461 shear of the equatorial oceanic current system and are observed in oceanic variables
462 such as SST [*Chelton et al.*, 2000]. TIWs modify the stability of the MBL, influencing
463 meridional and zonal wind [*Hayes et al.*, 1989; *Chelton et al.*, 2001; *Hashizume et al.*,
464 2002], as well as water vapor and boundary layer height [*Hashizume et al.*, 2002].
465 Pacific TIWs show significant amplitudes during the equatorial Eastern Pacific cold
466 season and disappear in the warm season, when the cold tongue vanishes [*Hayes et*
467 *al.*, 1989]. TIWs within the Galápagos archipelago have been previously reported
468 [*Sweet et al.*, 2009]. Wavelet spectral analysis of archive SST and wind data known to
469 display TIWs (e.g. [*Halpern et al.*, 1988]), as well as of data contemporary to the
470 PIQUERO and CHARLEX campaigns (SI, p.10), confirms that significant TIWs
471 passed through Galápagos during the CHARLEX campaign. The identification of the
472 17 and 33 day SST components with TIWs and the significant cross-power and
473 coherence between SST and O_3 in these bands (Fig. 6) in the equatorial Eastern
474 Pacific cold season suggest that the coupling of TWIs into the MBL may also result in
475 O_3 oscillations.

476 Fig. 8 shows that high SST coincides with a higher inversion and higher water content
477 of the MBL in 2000. These are effects of the coupling of SST TIWs to the MBL
478 structure previously found during the Shoyo-maru 1999 cruise [*Hashizume et al.*,
479 2002], although an impact on O_3 was not reported [*Shiotani et al.*, 2002] The cruise
480 track at 2° N intercepted several crests and troughs of the SST waves. The impact of
481 TIWs on the MBL was characterized by launching four radiosondes per day, but only
482 one in four was coupled to an ozonesonde. Fig. S12 (analogous to Fig. 8) shows
483 averaged vertical profiles for low (blue) and high (red) SST in the Shoyo-maru cruise
484 (thin lines) and in Galápagos (thick lines) during July-September 1999. It can be seen

485 how increase of the MBL height and decrease of O_3 mixing ratio during SST maxima
486 occur consistently in both datasets.

487 The generally antiphase relationship for the significant cross-power and coherence
488 intervals (Fig. 6), and the anti-correlation in the time domain of O_3 with SST and H_2O
489 mixing ratio suggest that the mechanism behind the impact of TIWs on O_3 may be
490 photochemical. However, understanding the intraseasonal variability of O_3 in relation
491 to meteorology is a complex topic requiring a detailed analysis of spatiotemporal
492 meteorological variability combined with CTM or CCM simulations. Such detailed
493 analysis is beyond the scope of this paper and will be subject of a follow-up study.

494 **4.3. Seasonal variability**

495 The seasonal pattern of surface O_3 at Galápagos is characteristic of the Southern
496 Hemisphere (SH), with a minimum in February and a maximum in August (see
497 annual cycles for Samoa, Ascension and Reunion in Fig. 11). Comparison of the
498 parameters of the Fourier series fit to the seasonal cycle to those of other locations
499 [*Parrish et al.*, 2016] highlights the similarity between Galapagos and Samoa,
500 including the annual average (y_0), the amplitude and phase of the first harmonic and
501 the low significance of the second harmonic. Barbados shows an analogous tropical
502 Northern Hemisphere (NH) behaviour, with a factor or ~2 higher annual average,
503 same amplitude and 6 months phase shift of the first harmonic, and low significance
504 of the second harmonic. The second harmonic in the MBL has been attributed by
505 [*Parrish et al.*, 2016] to photolytic loss of O_3, driven by the annual cycle of actinic
506 flux. The range of insolation experienced within the course of a year at low latitudes
507 is narrower than at higher latitudes, which explains why the second harmonic is less
508 significant in Galápagos.

509 However, the ozonesonde data shows the presence of a strong second harmonic aloft.
510 Fourier expansion fits of the seasonal cycles in Fig. 9*c* show that the first harmonic
511 has similar phase angle from the surface through the IL, albeit with decreasing
512 amplitude, becoming non-significant in the IL. The first harmonic is again significant
513 in the FT, but the phase and amplitude are completely different from those at the
514 surface. Both the amplitude and phase parameters of the second harmonic are similar
515 from the higher layers of the MBL through the FT. The inversion altitude annual
516 cycle (Fig. 9, panel *f*) is correlated to SST, with the strongest (and lower) inversions
517 occurring during the cold months (the maximum lapse rate at the inversion is also
518 plotted in panel *f*). All the radiosonde profiles indicate a capped MBL during the
519 August-November period (see T and RH climatological profile for September in Fig.
520 9, panels *a* and *c*). By contrast, in the warm season conditions compatible with
521 vertical exchange. Thus it can be concluded that in the warm period the MBL receives
522 influence of the FT, which causes a secondary maximum, whereas in winter the MBL
523 remains isolated from the FT. The double sinusoid in the FT cycle is an interesting
524 feature which should be addressed in future work. Analysis of FT O_3 in the Eastern
525 Pacific [*Kim and Newchurch*, 1996; *Oltmans et al.*, 2001] suggests that the maximum
526 in August-September results from transport of O_3-rich continental air masses during
527 the South-American biomass burning season, but the secondary maximum in January-
528 March has not been discussed yet.

529 The comparison between Galápagos and other tropical locations in Fig. 11 sheds light
530 into how the seasonal cycle of surface and MBL O_3 varies across the Equator. Open
531 ocean NH locations like, Cape Verde [*Lee et al.*, 2012], Barbados or Hawaii also have
532 a single sinusoidal annual cycle which describes the majority of the seasonal variation
533 [*Parrish et al.*, 2016], but with a maximum in January-April, i.e. ~6 months shifted

with respect to the SH cycle. The equatorial location of the Galápagos Islands does not lead to the surface O_3 seasonal cycle being an average between e.g. the cycles at Samoa (Pacific Ocean, 14 °S) and Barbados (Atlantic Ocean, 13 °N). The relative position of the ITCZ, which influences SST and wind (note that OLR, SST and wind components are plotted in Fig. 11 for each station), determines the surface O_3 seasonal cycle. Barbados is always north of the ITCZ, while the two Pacific locations are generally always at the southern side of it. Barbados is always under North Easterlies and Galápagos and Samoa generally always under South Easterlies. In July, the ITCZ is well north of the Equator and Barbados is at its northern edge. Under these circumstances the NE Trade Winds weaken and SST and water vapor concentration in the MBL are high, thus causing O_3 to decrease. At the same time the other two locations are far south of the ITZC and fully under SE Trade Winds, and therefore O_3 is high. The situation inverts in January, when the ITZC migrates south and both Galápagos and Samoa are at its southern edge. Samoa and Galápagos surface O_3 annual cycles are almost identical due to the ITCZ being curved towards the south in the Pacific Ocean and the situation of Galápagos at the north of the Pacific cold tongue, which implies higher levels of ozone upwind.

Fig. 11 shows measurements at two equatorial locations other than Galápagos. Paramaribo is half of the year at each side of the ITCZ and consequently displays a double O_3 maximum, with two minima occurring when the ITCZ passes above [*Maas*, 2004]. Kiritimati (Christmas Island, 2° N, 157° W), which is similarly situated than Galápagos with respect to the latitudinal shift of the ITCZ (see OLR cycle, Fig. 11), shows a hint of a surface O_3 seasonal cycle, at least according to the rather sparse data available [*Clarke et al.*, 1996; *Takashima et al.*, 2008; *Conley et al.*, 2011]. The likely explanation for a weaker seasonal cycle in Kiritimati than in Galápagos is that the

559 former is located at the tip of the Pacific cold tongue, with a dominating zonal wind
560 component and warm waters to the south, which essentially precludes the
561 replenishment of ozone-richer air from higher latitudes during austral winter-spring.
562 In October, O_3 is 10-15 ppbv at 10°S, 150° W [*Piotrowicz et al.*, 1986] and 20-30
563 ppbv at 10°S, 85° W [*Helmig et al.*, 2012]. Thus, the seasonal variation of the Pacific
564 cold tongue probably explains why the low O_3 region that extends across the
565 Equatorial Pacific in January-April becomes restricted to west of 150°W in July-
566 December [*Piotrowicz et al.*, 1986].

567 **4.4. Interannual variability**

568 Concurrent low SST and water vapor, and enhanced of O_3 occurred during the 2007
569 and 2010 La Niña events (Fig. 9). Before 2015 no major El Niño was registered in the
570 available O_3 record. The 2015-2016 El Niño has not caused extraordinary O_3
571 anomalies according to the few SHADOZ ozonesondes launched from San Cristóbal
572 in June-October 2015, with surface values of 13-20 ppbv during the Seasonal
573 maximum. These are slightly low but still larger than the values observed during the
574 cold season of 2011 (ENSO-neutral year). Thus, there seems to be a stronger response
575 of O_3 to low than to large SST anomalies in the longer time scales, although a clear
576 relationship is not apparent in the sparse data available.

577 **5. Summary and conclusions**

578 Continuous surface O_3 mixing ratios measurements at the Galápagos Islands in 2000-
579 2002 (PIQUERO campaign) and 2010-2012 (CHARLEX campaign) have been used
580 to identify modes of O_3 variability in different time scales ranging from a few days to
581 seasonal variations. The daily variability of surface O_3 at Galápagos has two distinct

582 regimes: *i*) a cycle of average photochemical destruction followed by night time
583 recovery in the cold season and *ii*) a pronounced cycle in the warm season
584 encompassing day-time advection and photochemical loss followed by night-time loss
585 associated with deposition and local NO_x emissions under windless conditions. On the
586 intraseasonal time scale, evidence of a possible impact of the 17 and 33 day period
587 TIWs on surface O_3 mixing ratios is reported for the first time. The impact of TIWs
588 throughout the MBL makes this environment particularly suitable for carrying out
589 quantitative studies on the O_3 budget and provides modelers with a challenging test
590 bed.

591 On the seasonal scale, it has been shown that Galápagos is situated in the chemical
592 SH, and that the change in the seasonal cycle in surface O_3 across the Equator
593 depends on the location with respect to the ITCZ, but also on the O_3 levels in the
594 subtropics. Galápagos is situated at the north of the Pacific cold tongue and as a
595 consequence does not display during austral winter and spring the low O_3 levels
596 observed in the Pacific warm pool at similar latitudes around the year [*Piotrowicz et*
597 *al.*, 1991].

598 **Acknowledgements**

599 CHARLEX was funded by the Spanish National Research Council (CSIC), the
600 Regional Government of Castilla-La Mancha and the National Institute of Aerospace
601 and Technology (INTA). The PIQUERO observations were supported by the
602 Innovative Research Program of the Cooperative Institute for Research in
603 Environmental Science (CIRES) at the University of Colorado. The authors are
604 grateful to Dora Gruber, the Harbor Master and Council of Puerto Villamil, the
605 Galápagos National Park and INAMHI for logistic support. M. V. Agama and J. F.

606 Paredes assisted in the launching of sondes and instrument maintenance. The MODIS
607 SST, O_3 profiles, buoy SST and winds, OLR and SST satellite climatologies, surface
608 O_3 at different locations, satellite wind data and in situ meteorological data at Santa
609 Cruz were obtained free of charge from the following web sites, respectively: NASA
610 Ocean Color (http://oceancolor.gsfc.nasa.gov/cms), SHADOZ
611 (http://croc.gsfc.nasa.gov/shadoz), TAO/TRITON (http://www.pmel.noaa.gov/tao),
612 NOAA/ESRL Physical Sciences Division (http://www.esrl.noaa.gov/psd),
613 NOAA/ESRL Global Monitoring Division (http://www.esrl.noaa.gov/gmd), SCOW
614 (http://cioss.coas.oregonstate.edu/scow) and Charles Darwin Foundation
615 (http://www.darwinfoundation.org). The wavelet software was developed by C.
616 Torrence and G. P. Compo and is available at the Web site of the Department of
617 Atmospheric and Oceanic Sciences of the University of Colorado
618 (http://paos.colorado.edu/research/wavelets). The wavelet cross-power and coherence
619 code was written by A. Grinsted (http://www.glaciology.net/wavelet-coherence). The
620 Shoyo-Maru data is available from the SOWER team upon request
621 (http://sower.ees.hokudai.ac.jp/data.html). The PIQUERO and CHARLEX datasets
622 are available from the authors upon request (voemel@ucar.edu, chmjgm@leeds.ac.uk,
623 a.saiz@csic.es).

Table 1. Multivariate linear regression analysis of the deseasonalized daily average O_3 time series (*n* data points; non-significant terms at 95% level for other variables are excluded).

	Variable	Coefficient	Std. Err.	*p*	*n*	R^2
PIQUERO	T	-12.6	1.7	0.0000	327	0.162
	RH	-2.3	0.3	0.0000		
	H_2O	84	11	0.0000		
	WS	0.55	0.18	0.0029		
01-02 COLD	H_2O	66	24	0.0064	239	0.160
	WS	1.23	0.22	0.0000		
	RH	-1.8	0.6	0.0045		
	T	-10	3	0.0026		
06/01-01/02 (C)	WS	1.0	0.3	0.0002	173	0.364
	RH	-2.9	0.6	0.0000		
	T	-16	3	0.0000		
	SST	-0.8	0.3	0.0145		
	H_2O	106	23	0.0000		
01-02 WARM	T	-25	7	0.0007	88	0.431
	RH	-5.2	1.5	0.0007		
	H_2O	170	40	0.0004		
	WS	-0.8	0.3	0.0117		
CHARLEX	H_2O	-6.7	1.0	0.0000	503	0.153
	v	0.40	0.18	0.0244		
	SST S. CRIST	-0.27	0.08	0.0009		
10-11 COLD [a]	H_2O	-5.8	1.9	0.0027	181	0.340
	v	1.0	0.4	0.0113		
	SST S. CRIST	-0.65	0.16	0.0001		
	Rad	0.015	0.003	0.0000		
10-11 COLD [a]	H_2O	-8.0	1.2	0.0000	330	0.234
	v	0.585	0.20	0.0036		
	SST S. CRIST	-0.37	0.09	0.0000		
09/10-01/11 (C)	H_2O	-8.08	1.70	0.0000	137	0.592
	v	1.5	0.3	0.0000		
	SST S. CRIST	-1.14	0.15	0.0000		
	Rad	0.013	0.002	0.0000		
	NO_2	9.6	1.9	0.0000		
07/11-01/12 (C)	H_2O	-5.6	1.5	0.0003	215	0.144
	SST S. CRIST	-0.24	0.10	0.0213		
	v	0.5	0.2	0.0199		

[a] Global radiation is not available for the full length of the campaign, and therefore only a subset of the cold season data can be regressed against this variable. For comparison, the results of regressing the complete cold season subset against the variables available are also shown.

References

Alpert, L. (1963), The climate of the Galapagos Islands, *Occ. Pap. Calif. Acad. Sci.*, *44*(8), 21-44.

Ayers, G. P., H. Granek, and R. Boers (1997), Ozone in the Marine Boundary Layer at Cape Grim: Model Simulation, *J. Atmos. Chem.*, *27*(2), 179-195.

Browell, E. V., et al. (2001), Large-scale air mass characteristics observed over the remote tropical Pacific Ocean during March-April 1999: Results from PEM-Tropics B field experiment, *J. Geophys. Res. [Atmos.]*, *106*(D23), 32481-32501.

Carpenter, L. J., S. M. MacDonald, M. D. Shaw, R. Kumar, R. W. Saunders, R. Parthipan, J. Wilson, and J. M. C. Plane (2013), Atmospheric iodine levels influenced by sea surface emissions of inorganic iodine, *Nature Geosci*, *6*(2), 108-111.

Chelton, D. B., F. J. Wentz, C. L. Gentemann, R. A. de Szoeke, and M. G. Schlax (2000), Satellite microwave SST observations of transequatorial tropical instability waves, *Geophys. Res. Lett.*, *27*(9), 1239-1242.

Chelton, D. B., S. K. Esbensen, M. G. Schlax, N. Thum, M. H. Freilich, F. J. Wentz, C. L. Gentemann, M. J. McPhaden, and P. S. Schopf (2001), Observations of Coupling between Surface Wind Stress and Sea Surface Temperature in the Eastern Tropical Pacific, *J. Clim.*, *14*(7), 1479-1498.

Clarke, A. D., Z. Li, and M. Litchy (1996), Aerosol dynamics in the equatorial Pacific marine boundary layer: Microphysics, diurnal cycles and entrainment, *Geophys. Res. Lett.*, *23*(7), 733-736.

Conley, S., et al. (2011), A complete dynamical ozone budget measured in the tropical marine boundary layer during PASE, *J. Atmos. Chem.*, *68*(1), 55-70.

de Laat, A. T. J., and J. Lelieveld (2000), Diurnal ozone cycle in the tropical and subtropical marine boundary layer, *J. Geophys. Res. [Atmos.]*, *105*(D9), 11547-11559.

Dickerson, R. R., K. P. Rhoads, T. P. Carsey, S. J. Oltmans, J. P. Burrows, and P. J. Crutzen (1999), Ozone in the remote marine boundary layer: A possible role for halogens, *J. Geophys. Res. [Atmos.]*, *104*(D17), 21385-21395.

Fabian, P., and P. G. Pruchniewicz (1977), Meridional distribution of ozone in the troposphere and its seasonal variations, *J. Geophys. Res.*, *82*(15), 2063-2073.

Gómez Martín, J. C., et al. (2013), Iodine chemistry in the Eastern Pacific marine boundary layer, *J. Geophys. Res. [Atmos.]*, *118*(2), 887–904.

Gregory, G. L., A. S. Bachmeier, D. R. Blake, B. G. Heikes, D. C. Thornton, A. R. Bandy, J. D. Bradshaw, and Y. Kondo (1996), Chemical signatures of aged Pacific marine air: Mixed layer and free troposphere as measured during PEM-West A, *J. Geophys. Res. [Atmos.]*, *101*(D1), 1727-1742.

Grinsted, A., J. C. Moore, and S. Jevrejeva (2004), Application of the cross wavelet transform and wavelet coherence to geophysical time series, *Nonlin. Processes Geophys.*, *11*(5/6), 561-566.

Halpern, D., R. A. Knox, and D. S. Luther (1988), Observations of 20-Day Period Meridional Current Oscillations in the Upper Ocean along the Pacific Equator, *J. Phys. Oceanogr.*, *18*(11), 1514-1534.

Hashizume, H., S.-P. Xie, M. Fujiwara, M. Shiotani, T. Watanabe, Y. Tanimoto, W. T. Liu, and K. Takeuchi (2002), Direct Observations of Atmospheric Boundary Layer Response to SST Variations Associated with Tropical

682 Instability Waves over the Eastern Equatorial Pacific*, *J. Clim.*, *15*(23), 3379-
683 3393.
684 Hayes, S. P., M. J. McPhaden, and J. M. Wallace (1989), The Influence of Sea-
685 Surface Temperature on Surface Wind in the Eastern Equatorial Pacific:
686 Weekly to Monthly Variability, *J. Clim.*, *2*(12), 1500-1506.
687 Helmig, D., E. K. Lang, L. Bariteau, P. Boylan, C. W. Fairall, L. Ganzeveld, J. E.
688 Hare, J. Hueber, and M. Pallandt (2012), Atmosphere-ocean ozone fluxes
689 during the TexAQS 2006, STRATUS 2006, GOMECC 2007, GasEx 2008,
690 and AMMA 2008 cruises, *J. Geophys. Res. [Atmos.]*, *117*(D4), n/a-n/a.
691 Hu, X.-M., J. Sigler, and J. Fuentes (2010), Variability of ozone in the marine
692 boundary layer of the equatorial Pacific Ocean, *J. Atmos. Chem.*, *66*(3), 117-
693 136.
694 Johnson, J. E., R. H. Gammon, J. Larsen, T. S. Bates, S. J. Oltmans, and J. C. Farmer
695 (1990), Ozone in the marine boundary layer over the Pacific and Indian
696 Oceans: Latitudinal gradients and diurnal cycles, *J. Geophys. Res. [Atmos.]*,
697 *95*(D8), 11847-11856.
698 Kim, J. H., and M. J. Newchurch (1996), Climatology and trends of tropospheric
699 ozone over the eastern Pacific Ocean: The influences of biomass burning and
700 tropospheric dynamics, *Geophys. Res. Lett.*, *23*(25), 3723-3726.
701 Komhyr, W. D. (1986), Operations handbook - Ozone measurements to 40-km
702 altitude with model 4A electrochemical concentration cell (ECC) ozonesondes
703 (used with 1680 MHz radiosondes), *Rep. 149*, 49 pp, NOAA Air Resources
704 Laboratory, Boulder, Colorado.
705 Komhyr, W. D., R. A. Barnes, G. B. Brothers, J. A. Lathrop, and D. P. Opperman
706 (1995), Electrochemical concentration cell ozonesonde performance
707 evaluation during STOIC 1989, *J. Geophys. Res. [Atmos.]*, *100*(D5), 9231-
708 9244.
709 Lee, J. D., S. J. Moller, K. A. Read, A. C. Lewis, L. Mendes, and L. J. Carpenter
710 (2009), Year-round measurements of nitrogen oxides and ozone in the tropical
711 North Atlantic marine boundary layer, *J. Geophys. Res. [Atmos.]*, *114*(D21).
712 Lee, T., G. Lagerloef, M. M. Gierach, H.-Y. Kao, S. Yueh, and K. Dohan (2012),
713 Aquarius reveals salinity structure of tropical instability waves, *Geophys. Res.*
714 *Lett.*, *39*(12), L12610.
715 Legeckis, R. (1977), Long Waves in the Eastern Equatorial Pacific Ocean: A View
716 from a Geostationary Satellite, *Science*, *197*(4309), 1179-1181.
717 Liu, S. C., M. McFarland, D. Kley, O. Zafiriou, and B. Huebert (1983), Tropospheric
718 NO x and O3 budgets in the equatorial Pacific, *J. Geophys. Res. [Oceans]*,
719 *88*(C2), 1360-1368.
720 Lyman, J. M., G. C. Johnson, and W. S. Kessler (2007), Distinct 17- and 33-Day
721 Tropical Instability Waves in Subsurface Observations*, *J. Phys. Oceanogr.*,
722 *37*(4), 855-872.
723 Maas, S. (2004), Boundary layer ozone and cloud coverage at Panamaribo Station
724 (5.8N 55.2W), *Rep. TR-264*, Koninklijk Nederlands Meteorologisch Instituut,
725 De Bilt, Netherlands.
726 MacDonald, S. M., J. C. Gómez Martín, R. Chance, S. Warriner, A. Saiz-Lopez, L. J.
727 Carpenter, and J. M. C. Plane (2014), A laboratory characterisation of
728 inorganic iodine emissions from the sea surface: dependence on oceanic
729 variables and parameterisation for global modelling, *Atmos. Chem. Phys.*,
730 *14*(11), 5841-5852.

731 Mahajan, A. S., et al. (2012), Latitudinal distribution of reactive iodine in the Eastern
732 Pacific and its link to open ocean sources, *Atmos. Chem. Phys.*, *12*(23), 11609-
733 11617.
734 McPhaden, M. J., et al. (2009), The Global Tropical Moored Buoy Array, paper
735 presented at OceanObs'09:Sustained Ocean Observations and Information for
736 Society, ESA Publication WPP-306, Venice, Italy.
737 Nagao, I., K. Matsumoto, and H. Tanaka (1999), Sunrise ozone destruction found in
738 the sub-tropical marine boundary layer, *Geophys. Res. Lett.*, *26*(22), 3377-
739 3380.
740 Oltmans, S. J., and H. Levy II (1994), Surface ozone measurements from a global
741 network, *Atmos. Environ.*, *28*(1), 9-24.
742 Oltmans, S. J., et al. (2001), Ozone in the Pacific tropical troposphere from
743 ozonesonde observations, *J. Geophys. Res.*, *106*(D23), 32503-32525.
744 Oman, L. D., J. R. Ziemke, A. R. Douglass, D. W. Waugh, C. Lang, J. M. Rodriguez,
745 and J. E. Nielsen (2011), The response of tropical tropospheric ozone to
746 ENSO, *Geophys. Res. Lett.*, *38*(13), L13706.
747 Paluch, I. R., S. McKeen, D. H. Lenschow, R. D. Schillawski, and G. L. Kok (1995),
748 Evolution of the Subtropical Marine Boundary Layer: Photochemical Ozone
749 Loss, *J. Atmos. Sci.*, *52*(16), 2967-2976.
750 Parrish, D. D., et al. (2016), Seasonal cycles of O3 in the marine boundary layer:
751 Observation and model simulation comparisons, *J. Geophys. Res. [Atmos.]*,
752 *121*(1), 538-557.
753 Piotrowicz, S. R., D. A. Boran, and C. J. Fischer (1986), Ozone in the boundary layer
754 of the equatorial Pacific Ocean, *J. Geophys. Res. [Atmos.]*, *91*(D12), 13113-
755 13119.
756 Piotrowicz, S. R., H. F. Bezdek, G. R. Harvey, M. Springer-young, and K. J. Hanson
757 (1991), On the ozone minimum over the equatorial Pacific Ocean, *J. Geophys.*
758 *Res. [Atmos.]*, *96*(D10), 18679-18687.
759 Prados-Roman, C., et al. (2015), Iodine oxide in the global marine boundary layer,
760 *Atmos. Chem. Phys.*, *15*(2), 583-593.
761 Randel, W. J., and A. M. Thompson (2011), Interannual variability and trends in
762 tropical ozone derived from SAGE II satellite data and SHADOZ
763 ozonesondes, *J. Geophys. Res.*, *116*(D7), D07303.
764 Read, K. A., et al. (2008), Extensive halogen-mediated ozone destruction over the
765 tropical Atlantic Ocean, *Nature*, *453*(7199), 1232-1235.
766 Reynolds, R. W., T. M. Smith, C. Liu, D. B. Chelton, K. S. Casey, and M. G. Schlax
767 (2007), Daily High-Resolution-Blended Analyses for Sea Surface
768 Temperature, *J. Clim.*, *20*(22), 5473-5496.
769 Saiz-Lopez, A., et al. (2012), Climate significance of halogen-driven ozone loss in the
770 tropical marine troposphere, *Atmos. Chem. Phys.*, *12*, 3939-3949.
771 Saiz-Lopez, A., R. P. Fernandez, C. Ordóñez, D. E. Kinnison, J. C. Gómez Martín, J.
772 F. Lamarque, and S. Tilmes (2014), Iodine chemistry in the troposphere and
773 its effect on ozone, *Atmos. Chem. Phys.*, *14*(23), 13119-13143.
774 Schultz, M. G., et al. (1999), On the origin of tropospheric ozone and NOx over the
775 tropical South Pacific, *J. Geophys. Res.*, *104*(D5), 5829-5843.
776 Shiotani, M., M. Fujiwara, F. Hasebe, H. Hashizume, Ouml, H. Mel, S. J. Oltmans,
777 and T. Watanabe (2002), Ozonesonde Observations in the Equatorial Eastern
778 Pacific -the Shoyo-Maru Survey-, *J. Meteorol. Soc. Jpn. Ser. II*, *80*(4B), 897-
779 909.

780 Smit, H. G. J., et al. (2007), Assessment of the performance of ECC-ozonesondes
781 under quasi-flight conditions in the environmental simulation chamber:
782 Insights from the Juelich Ozone Sonde Intercomparison Experiment (JOSIE),
783 *J. Geophys. Res. [Atmos.]*, *112*(D19), D19306.
784 Sorribas, M., J. C. Gómez Martín, T. D. Hay, A. S. Mahajan, C. A. Cuevas, M. V.
785 Agama Reyes, J. F. Paredes Mora, M. Gil-Ojeda, and A. Saiz-Lopez (2015),
786 On the concentration and size distribution of sub-micron aerosol in the
787 Galapagos Islands *Atmos. Environ.*, *123*, 39–48.
788 Sweet, W. V., J. M. Morrison, Y. Liu, D. Kamykowski, B. A. Schaeffer, L. Xie, and
789 S. Banks (2009), Tropical instability wave interactions within the Galápagos
790 Archipelago, *Deep Sea Res. Part I*, *56*(8), 1217-1229.
791 Takashima, H., M. Shiotani, M. Fujiwara, N. Nishi, and F. Hasebe (2008),
792 Ozonesonde observations at Christmas Island (2°N, 157°W) in the equatorial
793 central Pacific, *J. Geophys. Res.*, *113*(D10), D10112.
794 Thompson, A. M., et al. (1993), Ozone observations and a model of marine boundary
795 layer photochemistry during SAGA 3, *J. Geophys. Res. [Atmos.]*, *98*(D9),
796 16955-16968.
797 Thompson, A. M., et al. (2003), Southern Hemisphere Additional Ozonesondes
798 (SHADOZ) 1998-2000 tropical ozone climatology 2. Tropospheric variability
799 and the zonal wave-one, *J. Geophys. Res.*, *108*(D2), 8241.
800 Thompson, A. M., J. C. Witte, H. G. J. Smit, S. J. Oltmans, B. J. Johnson, V. W. J. H.
801 Kirchhoff, and F. J. Schmidlin (2007), Southern Hemisphere Additional
802 Ozonesondes (SHADOZ) 1998-2004 tropical ozone climatology: 3.
803 Instrumentation, station-to-station variability, and evaluation with simulated
804 flight profiles, *J. Geophys. Res.*, *112*(D3), D03304.
805 Thompson, A. M., S. J. Oltmans, D. W. Tarasick, P. von der Gathen, H. G. J. Smit,
806 and J. C. Witte (2011), Strategic ozone sounding networks: Review of design
807 and accomplishments, *Atmos. Environ.*, *45*(13), 2145-2163.
808 Torrence, C., and G. P. Compo (1998), A Practical Guide to Wavelet Analysis, *Bull.*
809 *Am. Meteorol. Soc.*, *79*(1), 61-78.
810 Wang, Y., et al. (2001), Factors controlling tropospheric O3, OH, NO x and SO2 over
811 the tropical Pacific during PEM-Tropics B, *J. Geophys. Res.*, *106*(D23),
812 32733-32747.
813 Wei, C. F., V. R. Kotamarthi, O. J. Ogunsola, L. W. Horowitz, S. Walters, D. J.
814 Wuebbles, M. A. Avery, D. R. Blake, E. V. Browell, and G. W. Sachse
815 (2002), Seasonal variability of ozone mixing ratios and budgets in the tropical
816 southern Pacific: A GCTM perspective, *J. Geophys. Res.*, *107*(D2), 8235.
817 Winkler, P. (1988), Surface ozone over the Atlantic ocean, *J. Atmos. Chem.*, *7*(1), 73-
818 91.
819 Ziemke, J. R., S. Chandra, L. D. Oman, and P. K. Bhartia (2010), A new ENSO index
820 derived from satellite measurements of column ozone, *Atmos. Chem. Phys.*,
821 *10*(8), 3711-3721.
822 Ziemke, J. R., A. R. Douglass, L. D. Oman, S. E. Strahan, and B. N. Duncan (2015),
823 Tropospheric ozone variability in the tropics from ENSO to MJO and shorter
824 timescales, *Atmos. Chem. Phys.*, *15*, 8037-8049.
825
826

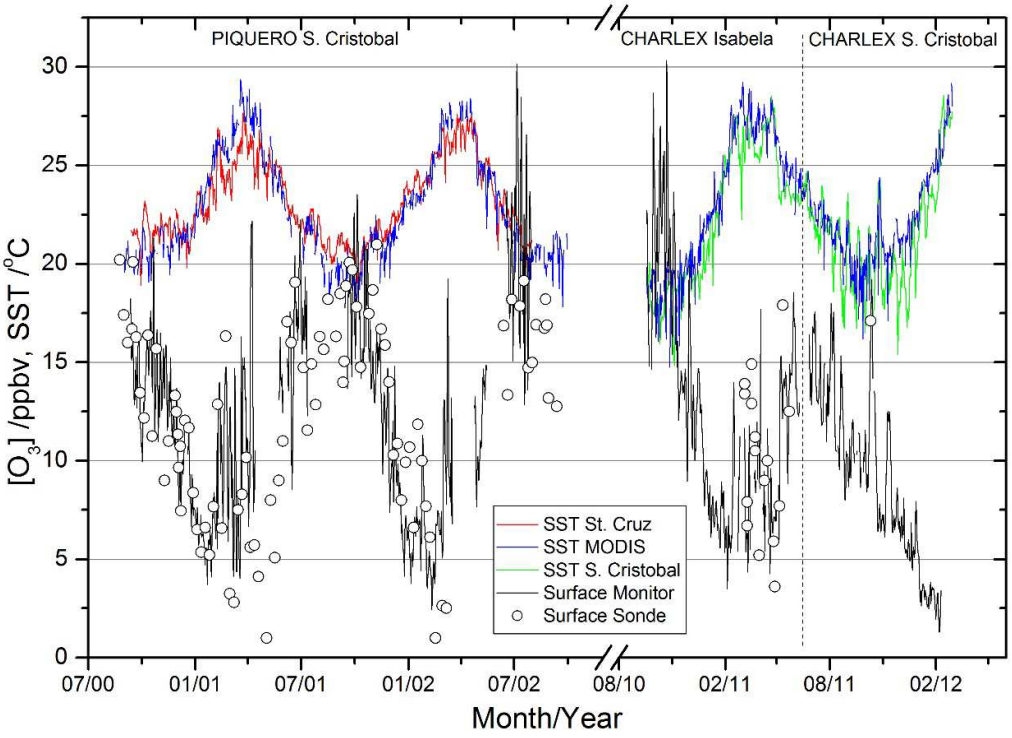

827

828 **Figure 1.** Daily averages of surface O_3 mixing ratios recorded during the PIQUERO
829 and CHARLEX campaigns (black line), concurrent ozonesonde surface
830 measurements (empty circles), and daily averaged sea surface temperature from
831 MODIS Aqua and Terra observations (blue) and from in situ measurements at Santa
832 Cruz (red) and San Cristóbal (green).

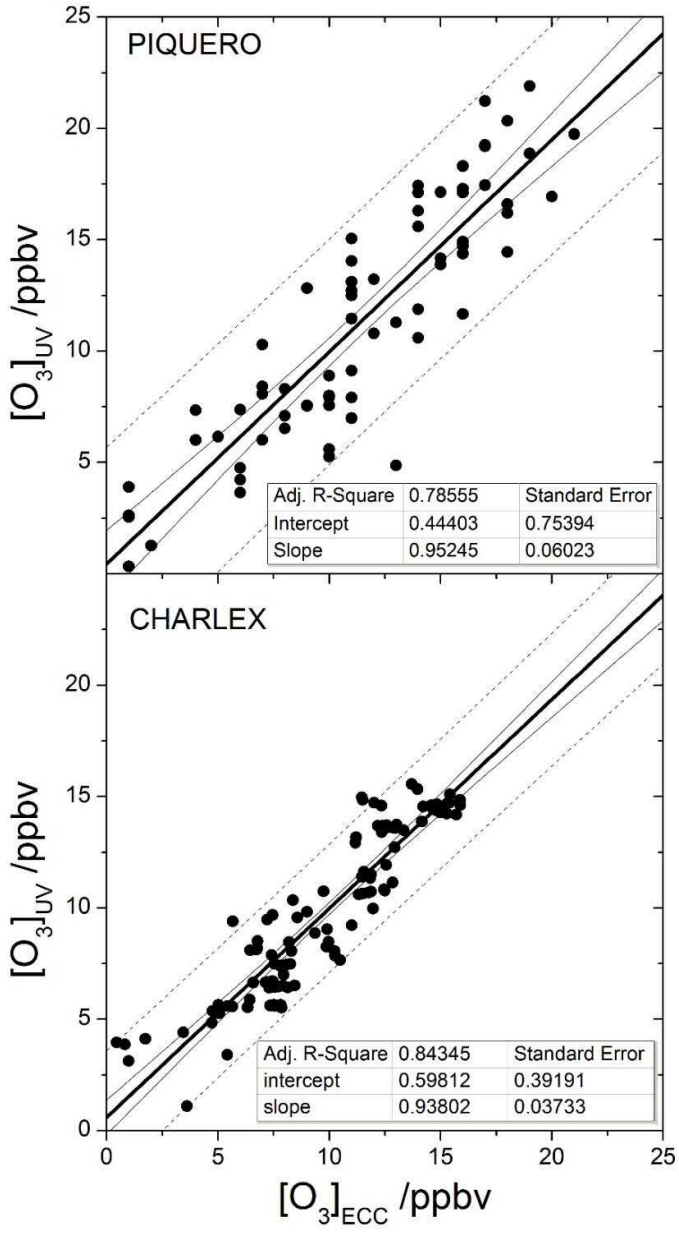

833

834 **Figure 2.** Correlation plots between UV and ECC surface measurements for
835 PIQUERO (top) and CHARLEX (bottom). Black lines are linear fits and dashed lines
836 the corresponding 95% prediction limits.

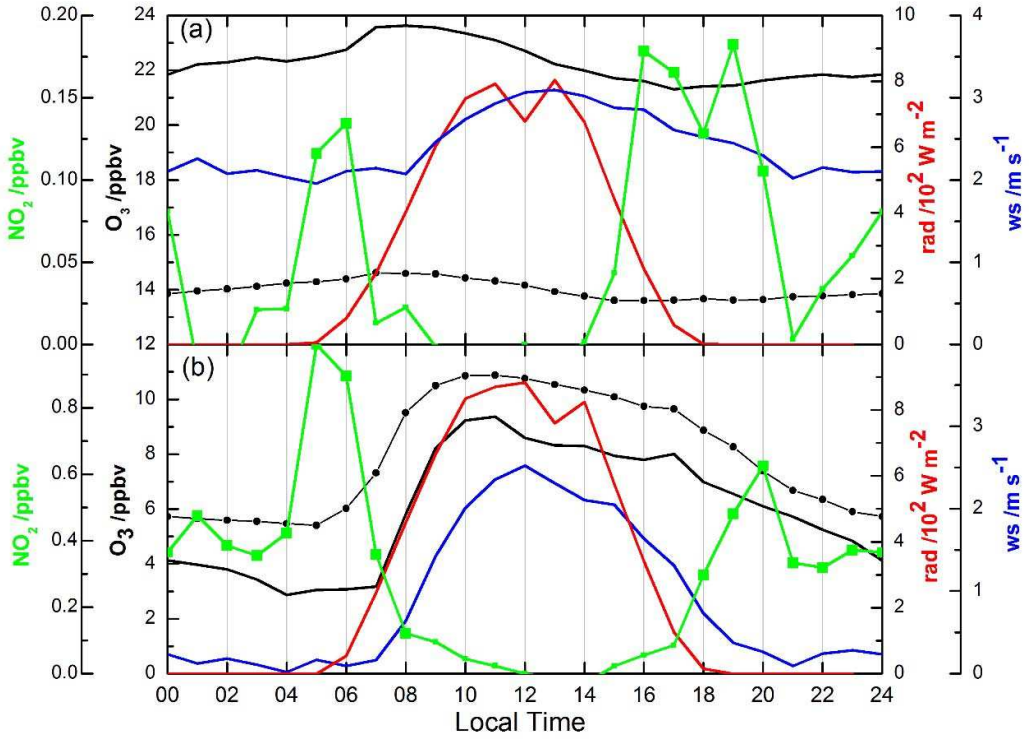

837

838 **Figure 3.** Monthly-averaged hourly values of surface O_3 (black), NO_2 (green
839 squares), global irradiance (red) and wind speed (blue) (the axes titles are color-
840 coded). The large squares represent NO_2 mixing ratios above the detection limit of the
841 instrument. Panel *a*: monthly averaged daily profiles for October 2010. The average
842 daily profile of O_3 of the two campaigns for September-November is represented by
843 the dotted black line. Panel *b*: monthly averaged daily profiles for February 2011. The
844 dotted black line represents here the average daily profile of O_3 for February-April.

845

846

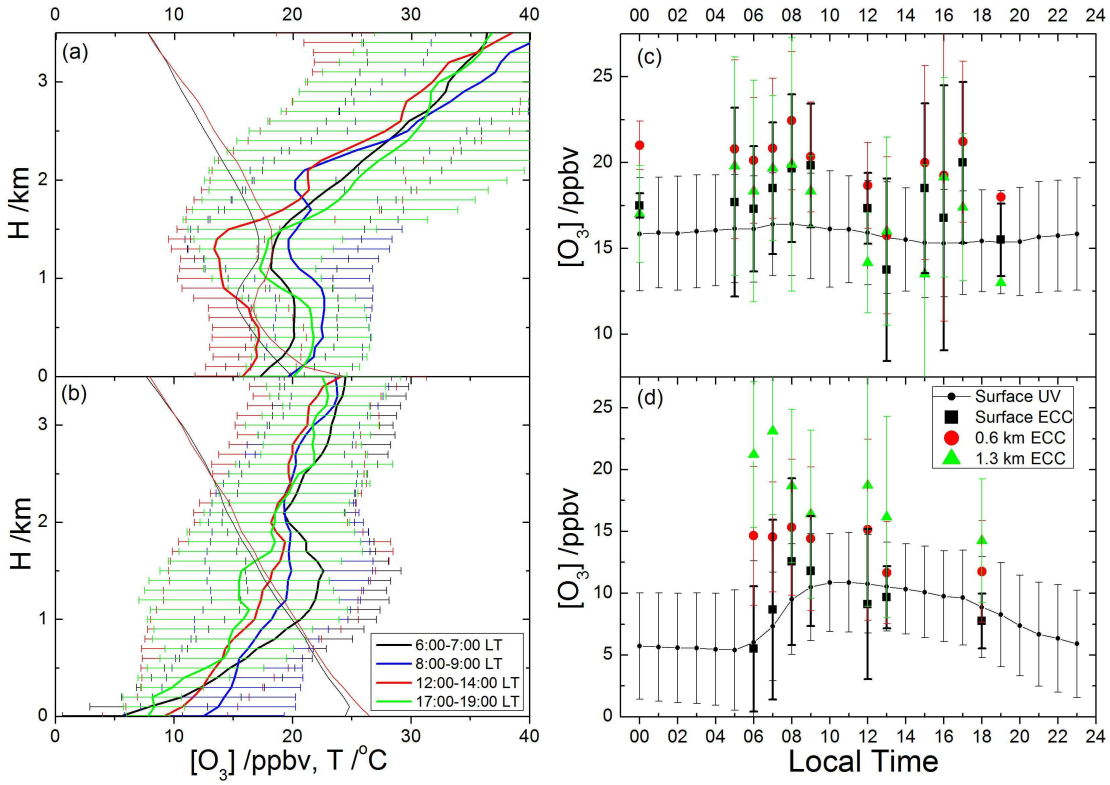

847

848 **Figure 4.** Panel *a*: August-October average vertical profiles for some of the most frequent
849 launching times of the SHADOZ database. Thick lines: O_3, thin lines: Temperature (for
850 simplicity only two temperature profiles out of four are shown). Panel *b*: the same for
851 February-April. Panel *c*: daily profiles at selected altitudes for August-October, plotted
852 alongside the surface UV average profile for September-October (no August data is available
853 for PIQUERO and CHARLEX). Panel *d*: the same for February-April.

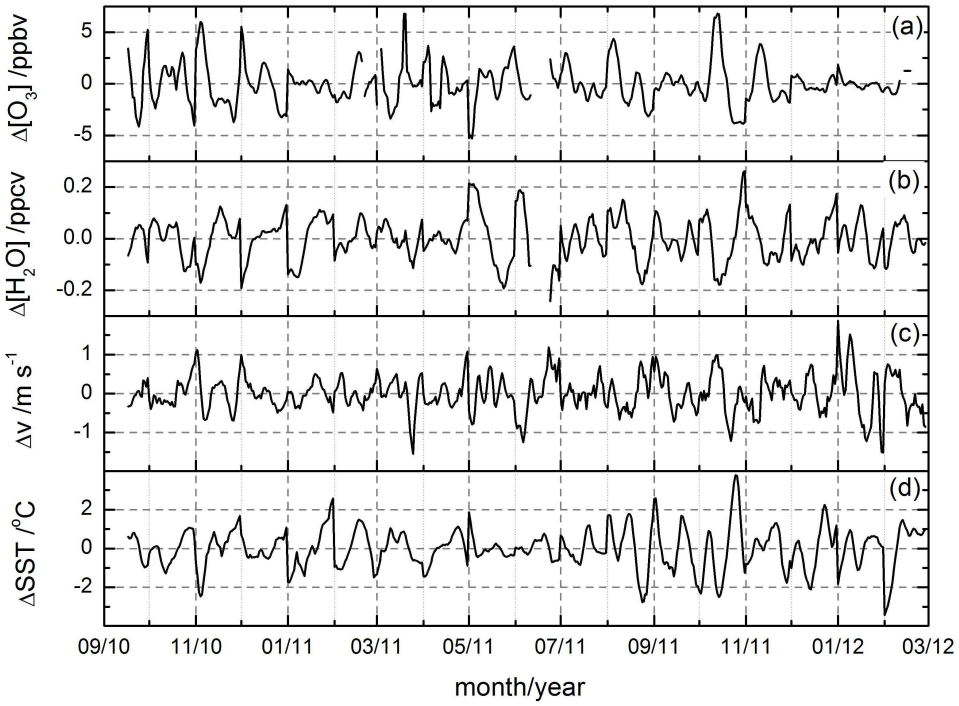

854

855 **Figure 5.** Deseasonalized, five day moving-averaged time series of O_3 mixing ratio
856 (panel *a*), water vapor mixing ratio (panel *b*) in parts per cent by volume, ppcv),
857 meridional wind component (panel *c*) and in situ SST (panel *d*) for the CHARLEX
858 campaign.

859

860

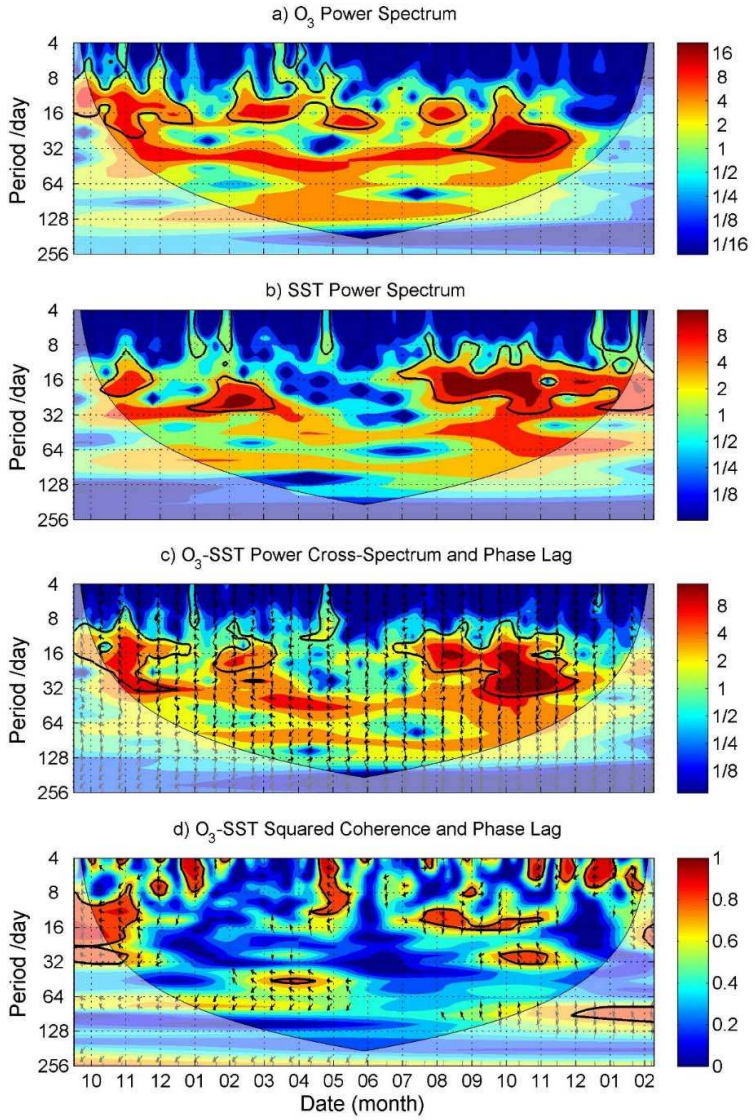

861

862 **Figure 6**. Wavelet power spectrum (using the Morlet wavelet) of surface O_3 mixing
863 ratio anomalies (*a*) and *in situ* SST (*b*) for the period 17/09/2010-31/01/2012
864 (CHARLEX campaign). Panel *c* shows the wavelet power cross-spectrum and panel *d*
865 the wavelet squared coherence of these two variables. The black contours denote the
866 95% a priori confidence limit with respect to red noise. The shaded areas indicate the
867 cone of influence, where edge effects might distort the picture. Arrows indicate the
868 phase lag between the two variables.

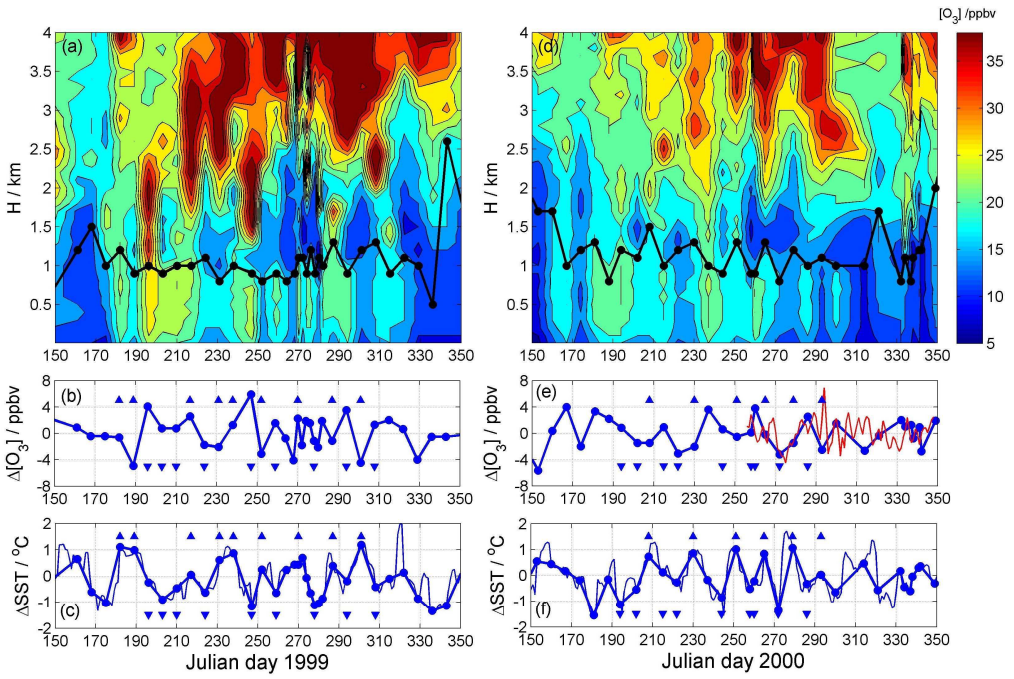

869

870 **Figure 7.** Vertical distribution of O_3 in the MBL and LFT during the cold season. Left
871 column (1999): O_3 mixing ratio contour plot and inversion altitude (black points)
872 from the SHADOZ record (panel *a*); surface O_3 anomalies from SHADOZ (panel *b*);
873 and satellite SST (panel *c*). Right column: the same for 2000; panel *b* also shows
874 surface O_3 anomalies from and PIQUERO in red. The satellite SST series have been
875 obtained from the NOAA OI SST V2 High Resolution Dataset by averaging 1/4°
876 pixels around San Cristóbal island. The SST concurrent with the ozonesonde
877 measurements are highlighted by blue dots connected with thick lines. The triangles
878 indicate which vertical profiles corresponding to high SST (▲) and low SST (▼)
879 anomalies are used to calculate the average vertical profiles shown in Fig. 8 (2000)
880 and Fig. S12 (1999).

881

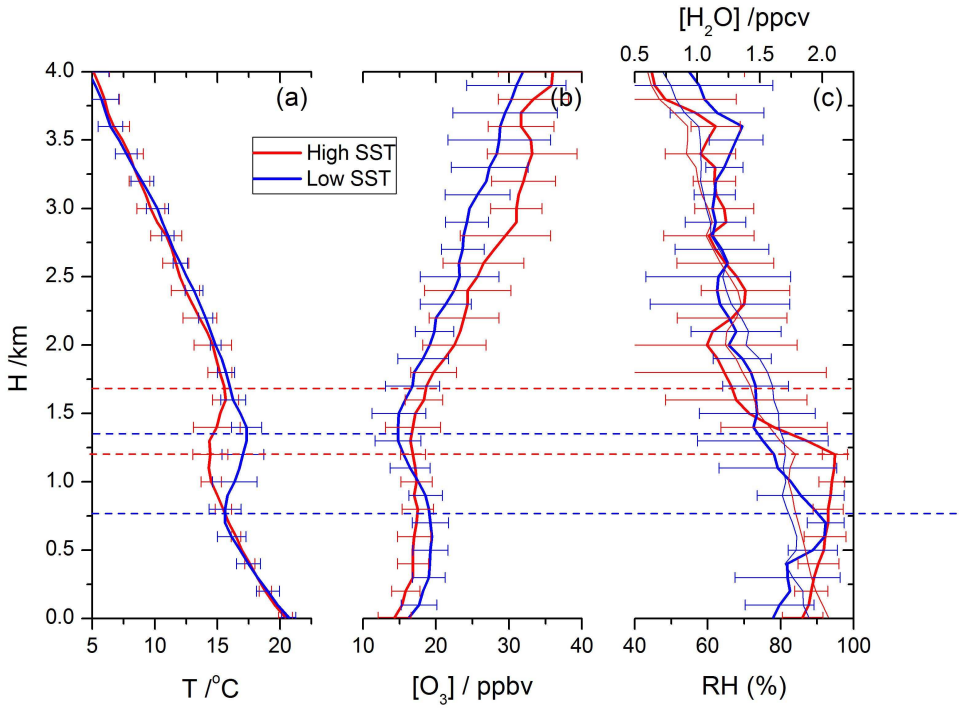

882

883 **Figure 8.** Average vertical profiles of temperature (panel *a*), O_3 mixing ratio (*b*),
884 relative humidity (*c,* bottom axis) and H_2O mixing ratio in parts per cent by volume
885 (*c*, top axis, thin lines) for positive (red) and negative (blue) SST anomalies in the
886 cold season of year 2000 (indicated by ▲ and ▼symbols in Fig. 7*f*). The blue (red)
887 dashed lines indicate the range of the inversion layer during negative (positive) SST
888 anomalies.

889

890

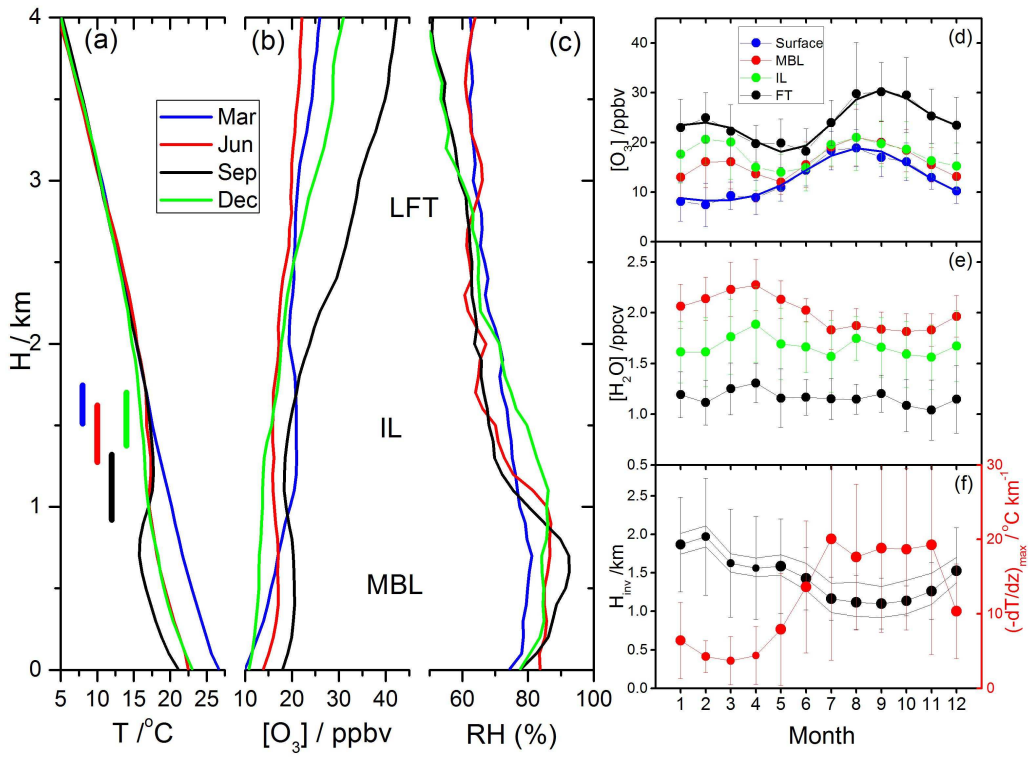

891

892 **Figure 9.** Average vertical profiles for the 1998-2014 period of temperature (*a*), O_3
893 (*b*) and relative humidity (*c*) for the months of March, June, September and December
894 during the 1998-2014 period, using SHADOZ and CHARLEX ozonesondes. The
895 vertical thick lines indicate the average thickness of the IL for the respective months
896 (see text for definition of the IL). The seasonal cycle of O_3 and water vapor averaged
897 over different layers (surface, average MBL, IL and LFT) are shown in panels *d* and
898 *e*, respectively. Fourier series expansion with to terms fitted to the O_3 seasonal
899 variation at the surface and the FT is shown in red in panel *d*. The seasonal variation
900 of the inversion altitude and maximum lapse rate at the inversion are plotted in panel *f*
901 (the size of the symbols indicates the fraction of capped MBL profiles relative to the
902 total number of sondes launched, with the largest size indicating 100%).

903

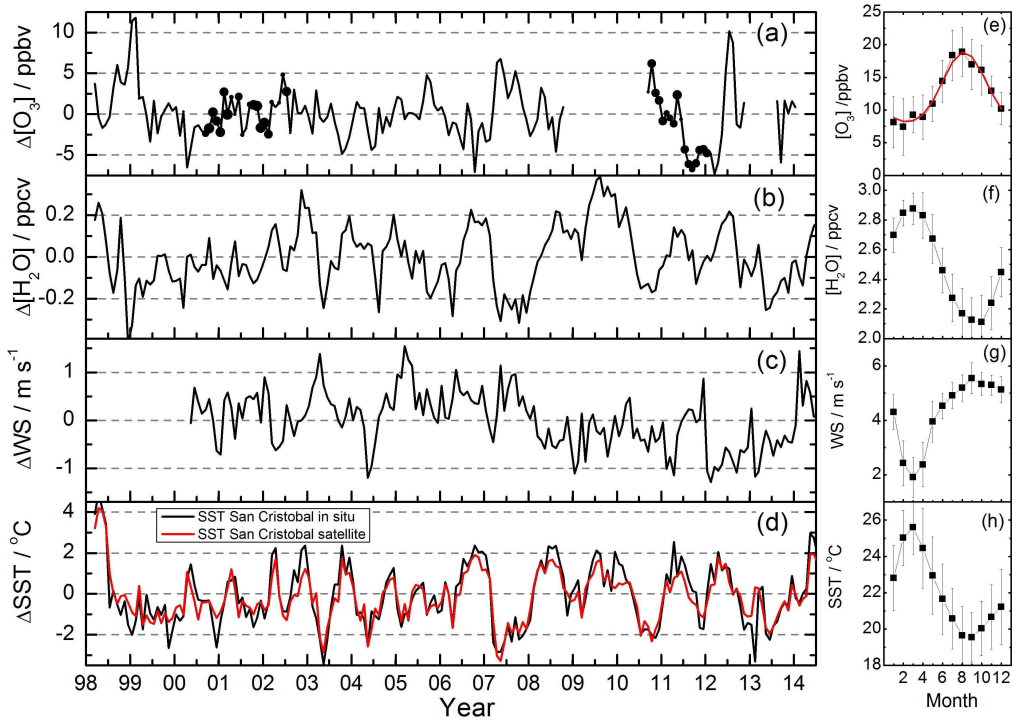

904

905 **Figure 10.** Monthly mean values of deseasonalized observations of O_3 (panel *a*) water
906 vapor (panel *b*), wind speed (panel *c*) and SST (panel *d*, in situ in black and satellite in
907 red). The small panels on the right column show the seasonal cycle of each variable.
908 A Fourier series expansion with to terms fitted to the O_3 seasonal variation is shown
909 in red in panel *e*. For the O_3 record (black dots in panel *a*), the size of the symbol is
910 scaled to the number of observations. During PIQUERO and CHARLEX the UV and
911 ECC data is averaged, and therefore the number of observations is much larger.

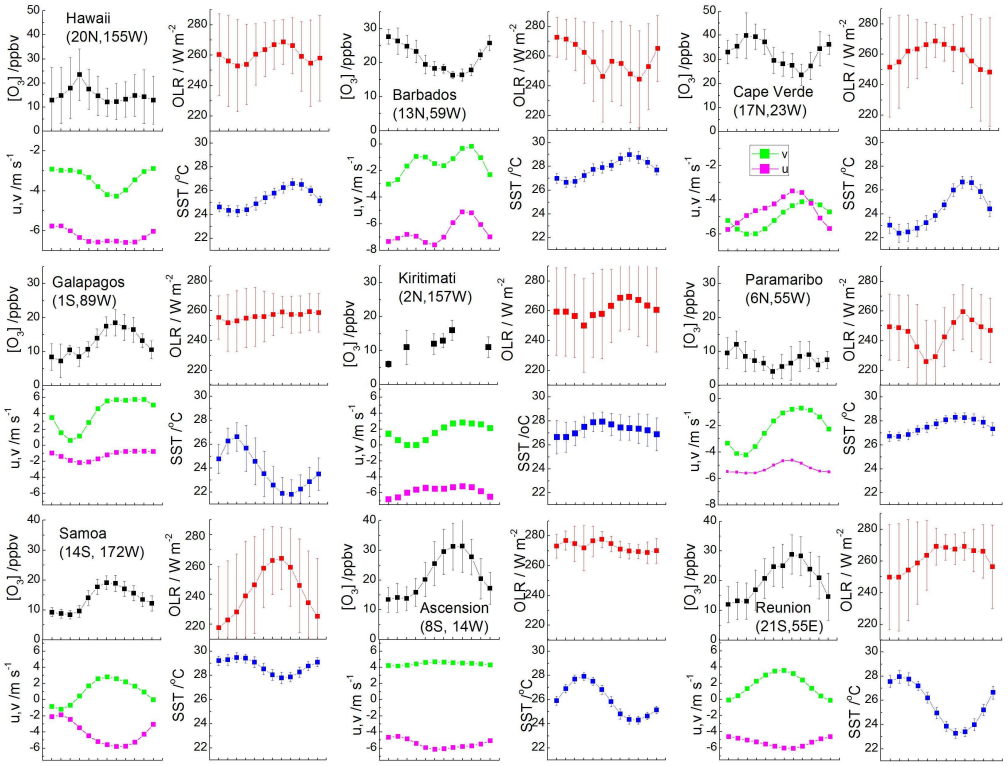

912

913 **Figure 11.** Seasonal cycle (January to December) of surface O_3, outgoing longwave
914 radiation (OLR) (NOAA), meridional (v) and zonal (u) wind (SCOW) and SST
915 (NOAA) for several remote ocean locations in the tropical Pacific, Atlantic and Indian
916 Oceans. Panels grouped in sets of four, one panel for each variable and one set for
917 each station. Multiyear O_3 data from SHADOZ (Galápagos, Ascension, Reunion) and
918 NOAA/ESRL (Hawaii, Samoa, Barbados). O_3 data at Kiritimati (Christmas Island)
919 from [*Clarke et al.*, 1996], [*Takashima et al.*, 2008] and [*Conley et al.*, 2011]
920 (different months from 1994 to 2007). O_3 data at Cape Verde (2007) from [*Lee et al.*,
921 2009]. O_3 data at Paramaribo (2003) from [*Maas*, 2004] and the STAR project
922 (http://projects.knmi.nl/star/intern/researchschool.htm)